# Size-Dependent Ultrafast Charge Carrier Dynamics of WO$_3$ for Photoelectrochemical Cells

Kevin P. Regan, Christopher Koenigsmann, Stafford W. Sheehan, Steven J. Konezny, and Charles A. Schmuttenmaer*

Department of Chemistry and Yale Energy Sciences Institute, Yale University, New Haven, Connecticut 06520-8107, United States

S *Supporting Information*

ABSTRACT: Time-resolved terahertz (THz) spectroscopy and open-circuit photovoltage measurements were employed to examine the size-dependent charge carrier dynamics of tungsten(VI) oxide (WO$_3$) particles for their use as the photoanode in photoelectrochemical cells. Specifically, films of commercially available WO$_3$ nanoparticles (NPs) and granular particles (GPs) with diameters of 77 ± 34 and 390 ± 260 nm, respectively, were examined in air and while immersed in 0.1 M Na$_2$SO$_4$ electrolyte (pH = 2). Examination of the frequency-dependent transient photoconductivity at short and long time scales indicates the presence of both photoinduced high net transport charge carriers at early times and in some cases low net transport charge carriers at later times. The high net transport charge carriers dominate the photoconductivity signal for ~100 ps after photoexcitation. Depletion of the short-lived high net transport carriers due to trapping leads to the detection of longer-lived low net transport photoinduced charge carriers that likely contribute to surface chemistry.
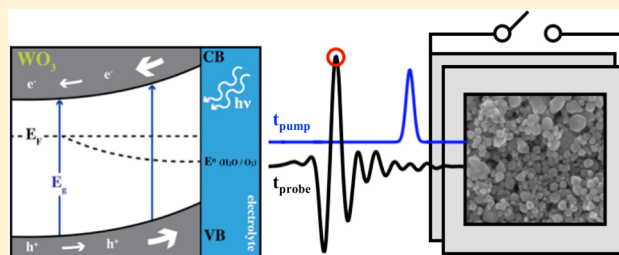
INTRODUCTION

Photoelectrochemical cells (PECs) convert solar energy into either electrical power or a fuel, and their optimization is a promising pathway in the development of renewable energy sources.[1−3] Metal oxide semiconductors have been widely studied for their application in water splitting cells due to their favorable structural and electronic properties.[4−7] Tungsten(VI) oxide (WO$_3$) is of particular interest because it has a relatively small band gap energy of 2.6 eV (corresponding to a wavelength of 475 nm), enabling it to absorb light in the visible spectrum without the need for sensitizer dyes.[8,9] Its electrochemical properties[10,11] and spectroscopic properties, including transient absorption[12−14] and time-resolved microwave spectroscopy,[15] have been studied previously. However, ultrafast photoinduced charge carrier dynamics in WO$_3$ have not yet been investigated on the picosecond time scale. Our interests lie in the characterization and dynamics of the nascent photoinduced carriers that are required for efficient oxidation at the metal oxide/electrolyte interface.

We examine for the first time ultrafast photoinduced carrier dynamics in WO$_3$ particles as a function of particle size utilizing optical pump−THz probe (OPTP) spectroscopy. THz measurements were performed under open-circuit conditions on as-prepared dry films in air as well as in the presence of the aqueous electrolyte employed during photocatalysis in order to gain insights into the ultrafast dynamics under near-operating conditions. The spectroscopic results, including measurements of photoinduced charge carrier lifetimes and the frequency-dependent complex transient photoconductivity, are also correlated with open-circuit photoelectrochemical measurements of two WO$_3$ particle sizes.

EXPERIMENTAL METHODS

Preparation of WO$_3$ Films. The method described by Grätzel and co-workers for the preparation of TiO$_2$ NP pastes[16] was optimized for the fabrication of WO$_3$ nanoparticle (NP) and granular particle (GP) pastes employed herein. Pastes were prepared from commercially available WO$_3$ nanoparticles (WO$_3$ NPs, Sigma-Aldrich, <100 nm nanopowder, Lot #: MKBN9123V) and granular particles (WO$_3$ GPs, Sigma-Aldrich, ≤20 μm powder, ≥99%, Lot #: MKBH5583V). The as-received WO$_3$ powders were ground in the presence of glacial acetic acid (JT Baker, ACS Reagent), α-terpineol (Alfa Aesar, 96%), water, and ethanol for a period of 45 min. The resulting slurry was diluted with a solution consisting of 10 and 22 cPs of ethyl cellulose (Acros Organics, 48% ethoxyl content) dissolved in a 1:1 ratio and homogenized with sonication. The paste was concentrated by rotary evaporation to produce a homogeneous paste of the WO$_3$ powder, which was stable from precipitation for up to two months.

Uniform, transparent films of the WO$_3$ particles were deposited onto the surface of quartz substrates (GM Associates, fused quartz, 25.4 mm × 25.4 mm). To improve the adhesion of the films, the surface of the quartz substrates was abraded with 600 grit sandpaper (3M) and then immersed into a

solution consisting of 70% sulfuric acid (JT Baker, ACS reagent) and 30% hydrogen peroxide (JT Baker, 30% v/v in water, ACS Reagent). The treated substrates were then rinsed with ultrapure (18.2 MΩ·cm) water to remove excess acid. The deposition of the films was accomplished by the doctor blading method. After each deposition step, the films were heated at 80 °C before the deposition of a subsequent layer or before annealing. The films were sintered by annealing at 470 °C for a period of 30 min. The resulting films were highly transparent with reproducible thicknesses (Figure S1) of approximately 1, 2.5, and 3−3.5 μm after deposition of 1, 2, and 3 layers of the paste, respectively. The high degree of transparency and the uniformity of the WO_3 particle films represent an important step toward generating films with applications in integrated photoelectrochemical water-splitting devices. However, the pastes and resulting films reported herein were optimized for characterization by THz spectroscopy. Thus, further improvements in electrochemical performance are expected upon optimization of the paste to increase surface area and porosity, but this is beyond the scope of this report. Details regarding the characterization of the WO_3 nanoparticles including electron microscopy, X-ray diffraction, diffuse reflectance spectroscopy, electrochemistry, and dc conductivity measurements are found in the Supporting Information.

Time-Resolved THz Spectroscopy. THz radiation is generated from a plasma source seeded by an amplified Ti:sapphire laser,[17] as seen in Figure S5. The amplifier (Spectra-Physics Spitfire Ace) emits 4 W of pulsed 35 fs, horizontally polarized, 800 nm light at a 1 kHz repetition rate. The beam is then split into the optical pump beam and THz generation and detection beams. Transmitted 800 nm light is frequency doubled to 400 nm light using a Type I β-barium borate (BBO) crystal (Eksma Optics), which serves as the optical pump beam to photoexcite the sample for OPTP spectroscopy.[18,19] The remainder is used to generate the THz pulse and profile the THz electric field as a function of time. The generation beam is transmitted through a beam sampler where it produces THz radiation via plasma generation in air,[20] and a small portion (∼10%) is reflected and serves as the detection beam for free space electro-optic sampling in a ZnTe (110) crystal. A delay stage on the generation beam allows for acquisition of a time-domain spectrum of the THz pulse. Transient photoconductivity of WO_3 NP and GP films was calculated using the thin-film approximation.[21] The samples were photoexcited with 400 nm light at both 100 and 200 mW of power and a beam diameter of 7 mm, yielding a pump fluence, F, of 260 and 520 μJ/cm², respectively. The time-domain THz pulse transmitted through the nonphotoexcited WO_3 sample, and at a specific pump delay times, t_{pump}, were measured. More detailed information on this technique has been presented previously.[18,22−24]

■ RESULTS AND DISCUSSION

Characterization of WO_3 Films. The only differences between the NPs and GPs are their overall size, and the fact that the GPs are polycrystalline with grain sizes that are smaller than those of the NPs. X-ray powder diffraction (XRD) patterns collected from the sintered films (Figure 2e) confirmed that the WO_3 NP and GP films are (poly)crystalline and comprise the catalytically active monoclinic phase.[25] No crystalline impurities were detected. The relative grain size in the GPs and NPs was determined by comparing the full width at half-maximum (fwhm) of the (111) reflection at $2\theta = 26.6°$.

The fwhm of the NPs (0.316°) is 20% smaller than that of the GPs (0.392°).

Scanning electron microscopy (SEM) and transmission electron microscopy (TEM) were performed on the sintered samples to investigate the structure of the films and individual particles. The SEM images (Figure 1) reveal that NP and GP
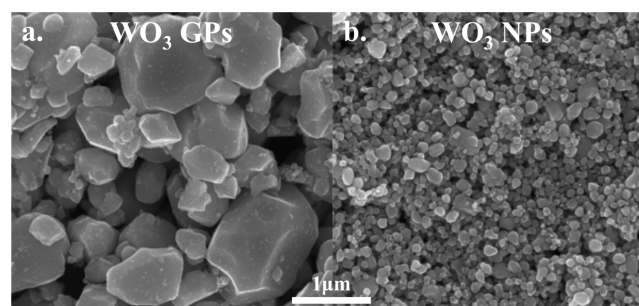

Figure 1. SEM images of ∼3 μm thick films of WO_3 NPs (a) and GPs (b).

samples consist of particles with average diameters of 77 ± 34 and 390 ± 260 nm, respectively. Particle size histograms shown in Figure S2 highlight the polydispersity of particle sizes in the GP sample. The TEM images shown in Figure 2 further highlight the morphology of the NPs and GPs. High-resolution TEM images reveal that the NPs are essentially single crystalline, whereas the GPs are polycrystalline and consist of multiple grains with relatively small diameters. This is consistent with the XRD results, which indicate that the grains in the NPs are smaller than those in the GPs.

Diffuse reflectance spectra (Figure S3) show that the GP and NP films absorb light strongly in the visible region of the spectrum. The optical band gaps are nearly identical for the NPs and GPs and were determined to be 2.59 and 2.61 eV, respectively. In order to quantitatively compare the surface electronic properties of each sample, their flat-band potentials were determined. The flat-band potential quantifies the potential drop in the interfacial space-charge region by measuring the externally applied voltage which results in no band bending. The flat-band potentials for the NPs (0.608 V vs RHE) and GPs (0.602 V vs RHE) are nearly equal, which indicates that the potential drop in the space-charge region of the NP and GP films is the same and provides evidence that their surfaces are electronically equivalent (Figure S8).

Overall, our analysis reveals that the only significant differences between the NPs and GPs are the relative size of the particles and relative size of crystalline grains. This was further verified by determining the ambient conductivity of the WO_3 NP and GP films (additional details for this technique can be found in the Supporting Information). It was found that the dc conductivity of the NP film (9.8×10^{-6} S/cm) was more than 40-fold larger than the GP film (2.3×10^{-7} S/cm). The lower conductivity in the GP film is consistent with the larger diameter of the particle and their polycrystalline morphology. The relatively large diameter of these particles reduces the interparticle contact (cf. Figure 1) producing fewer conduction pathways through the GP films. Moreover, individual GPs consist of many small crystallites connected by grain boundaries, which also contributes to higher resistivity.[26] On the other hand, the NP films consist of a highly interconnected mesoporous network of single-crystalline particles, which
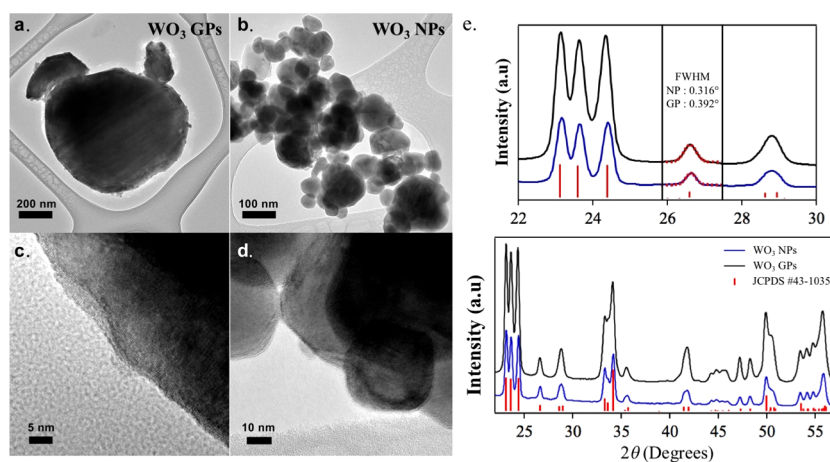
Figure 2. HRTEM and XRD analysis of WO$_3$ Films. (a) HRTEM of WO$_3$ GPs and a magnified view (c) to depict the crystal lattice. (b) HRTEM of WO$_3$ NPs and a magnified view (d) to show the crystal lattice. (e) XRD spectra of the WO$_3$ NPs (blue) and the GPs (black) where the red lines correspond to the JCPDS of WO$_3$. A Gaussian was fit to the isolated peak at $2\theta = 26.6°$ to determine the peak widths of the NPs and the GPs (top panel).

provides a much more expansive network of conduction pathways throughout the film.

Ultrafast Spectroscopic Measurements. Ultrafast optical pump–THz probe spectroscopy (OPTP) was employed to determine the photoinduced mobile charge carrier lifetime in WO$_3$. THz radiation is sensitive to the product of concentration and mobility of electrons and holes, i.e., the sample's conductivity. The arrival of the THz probe pulse is delayed with respect to the arrival of the 400 nm optical pump pulse over a range of −5 to 900 ps. The THz probe pulse is attenuated by mobile charge carriers in the valence and conduction bands of the WO$_3$, which enables measurement of the rate and magnitude of carrier generation and trapping upon photoexcitation. OPTP measurements were performed under open-circuit conditions in air and 0.1 M Na$_2$SO$_4$ (pH = 2) electrolyte used for photoelectrochemical measurements (shown schematically in Figure 4c). The introduction of electrolyte allows for the determination of carrier trapping dynamics under circumstances similar to operating conditions. Photoinduced carrier dynamics were investigated in two ways: The first was to characterize the overall conductivity decay dynamics due to filling of trap states at grain boundaries and the metal oxide/dielectric interface, and the second was to determine the frequency-dependent complex-valued conductivity measured at three different time delays after photoexcitation. We find that long-lived charge carriers may exist for 900 ps or longer, and these long-lived photoinduced carriers result in a vertical offset of the OPTP trace at long times.

Trapping occurs when photoinduced charge carriers fall into low mobility states that are not detected by THz radiation. Because of the inhomogeneity of the mesoporous films, we attribute the mobile charge trapping in the WO$_3$ as a distribution of lifetimes as opposed to a single or few lifetimes. This type of trapping dynamics are best represented by the Kohlrausch–Williams–Watts (KWW) function, which is commonly referred to as a stretched exponential.[11] The change in the peak amplitude of the THz pulse as a function of time after the pump pulse, t_{pump}, is described as a stretched exponential decay with an offset convoluted with a Gaussian instrument response function:

$$-\Delta\text{THz} = \left[A \exp\left(-\frac{t_{pump} - t_0}{\tau} \right)^{\beta} + y_0 \right] \otimes G_R(\text{fwhm})$$

(1)

where A is the amplitude, t_0 is the time at which the pump pulse arrives, τ is the time constant of the stretched exponential, β is the stretching parameter ($0 < \beta < 1$), y_0 is the long-time offset, $\otimes$ represents a convolution, and $G_R(\text{fwhm})$ is a Gaussian with a specified full width at half-maximum representing the instrument response function.

The average lifetime of the carriers in the system, $\langle\tau\rangle$, is proportional to the area underneath the stretched exponential curve, i.e., $\int_0^\infty \exp(-t/\tau)^\beta \, dt$, and is determined from τ and β using the analytical expression

$$\langle\tau\rangle = \frac{\tau}{\beta}\Gamma\left(\frac{1}{\beta}\right)$$

(2)

where Γ is the gamma function.

The stretched exponential trapping dynamics (∼100 ps time scale) provide insight into the concentration of initial photoinduced mobile charges that are rapidly trapped at the surface and grain boundaries within the WO$_3$. In previous studies, it was determined from spectroscopic measurements on the picosecond time scale that the rate of electron trapping was on the order of 100 ps,[12] while the rate of recombination was on the order of several hundred nanoseconds. For example, time-resolved microwave conductivity studies have found that ∼80% of recombination occurs in WO$_3$ within 500 ns.[15] In this study, we measure the dynamics on the picosecond time scale (<∼1 ns), and thus, we believe that the stretched exponential decay can be primarily attributed to carrier trapping.

It is seen in Figure 3 that the trapping dynamics exhibited in the WO$_3$ NPs and GPs are qualitatively similar except for the fact that the NPs retain a larger fraction of the initial charge carriers over a 100 ps time window. The best-fit parameters of eq 1 to the eight data sets in Figure 3 are presented in Table S1 along with their associated uncertainty values.

The trapping dynamics exhibit instrument response limited dynamics at the earliest time scales. Therefore, a Gaussian instrument response function, $G_R(\text{fwhm})$, was convoluted with a stretched exponential function and long-time offset (eq 1) to
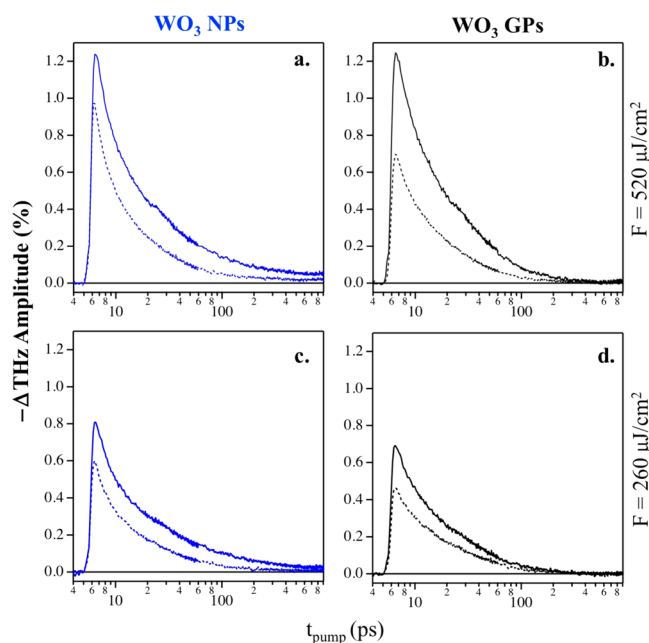
Figure 3. OPTP measurements of bare (dotted line) and electrolyte-sealed (solid line) WO$_3$ NPs (blue) and GPs (black) films. Traces were taken at both 520 μJ/cm^2 (first row) and 260 μJ/cm^2 (second row) pump fluence, F.

accurately determine the underlying amplitude parameter, A, for each trace. Three separate samples were made for each of the eight permutations of bare/electrolyte, NP/GP, and 260 μJ/cm^2/520 μJ/cm^2, and each was fit individually to determine the average and standard deviation for the fit parameters of eq 1. The size-dependent nature of the WO$_3$ NPs and GPs and dielectric influence can be succinctly described with a single term $A\langle\tau\rangle$, which corresponds to the product of carrier density and average lifetime of highly mobile charge carriers after photoexcitation. This can be thought of as the time-integrated carrier density, and it incorporates the A, β, and τ values extracted from fitting eq 1 (cf. Supporting Information).

The introduction of aqueous electrolyte to both systems results in a marked increase in the average lifetime of highly mobile carriers in the system using pump fluence of both 260 and 520 μJ/cm^2, as seen in Figures 3 and 4a. Physically, changing the environment surrounding the film from air to aqueous electrolyte not only affects the dielectric constant of

medium but also results in changes to the WO$_3$ surface including passivation, hydration, and protonation/deprotonation.[27] The modification of the particle's surface chemistry likely plays a significant role in the average lifetime of mobile charge carriers in both the NPs and GPs. In air, low-coordination atoms at the surface of the particles are known to act as trap sites for charge carriers. In the presence of electrolyte, these low-coordination atoms are passivated by the electrolyte decreasing the density of surface traps.[28] Since the NPs have a higher surface area to volume ratio than the GPs, the passivation of surface traps is expected to have a larger impact on the lifetime of the carriers in the NPs compared to the GPs.

In addition, the NPs are essentially single crystalline so the majority of traps are expected to be localized at the surface. On the other hand, the GPs are polycrystalline so there is a combination of both surface traps and traps at the grain boundaries between individual crystallites within a particle. These factors decrease the effect of surface passivation on carrier trapping in GPs since grain boundaries within the core of the particle are unaffected by the presence of an electrolyte. This is consistent with the fact that we find a larger change in the average lifetime of the NPs than the GPs upon addition of electrolyte.

Transient Photoconductivity of WO$_3$. The frequency-dependent complex-valued transient photoconductivity was measured in order to further investigate size-dependent ultrafast carrier dynamics in the WO$_3$ particles. At pump delay times of $t_{pump} = 0$ and 12 ps, the transmitted THz pulse was collected under nonphotoexcited and photoexcited conditions, and the transient photoconductivity of the NP and GP films was determined using the thin-film approximation.[16] At these short time scales, we determined the frequency-dependent conductivity for the NPs and GPs in both the bare and electrolyte-sealed configurations. However, at longer delay times ($\sim$600 ps), we were only able to measure the conductivity of the NP sample in aqueous electrolyte with 520 μJ/cm^2 excitation fluence since this was the only one to have a significant signal at delay times greater than 200 ps (Figure 7a). The Drude−Smith model was used to describe the frequency-dependent complex conductivity:[29,30]

$$\hat{\sigma}(\omega) = \frac{Ne^2\tau_{scatt}/m^*}{1 - i\omega\tau_{scatt}}\left(1 + \frac{c_1}{1 - i\omega\tau_{scatt}}\right) \qquad (3)$$
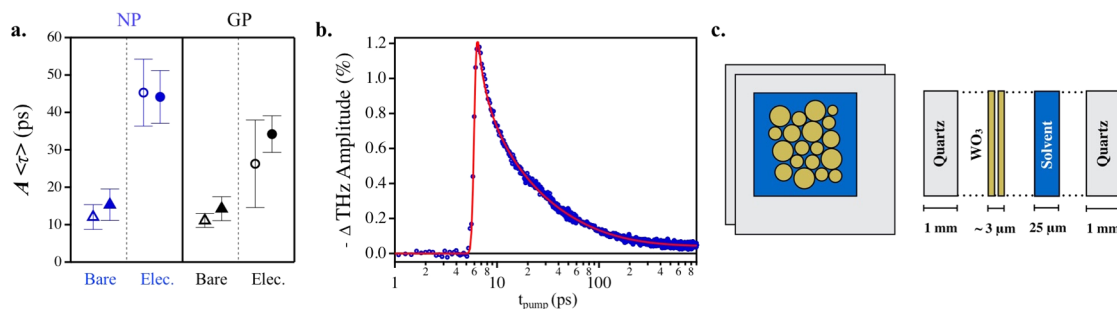
Figure 4. Ultrafast trapping dynamics of bare (triangles) and electrolyte-sealed (circles) WO$_3$ films. Part (a) depicts the relative concentration of mobile charges from the best fit parameters for the stretched exponential trapping dynamics of WO$_3$ NPs (blue) and GPs (black). The parameters for data taken at 260 μJ/cm^2 pump fluence are shown with open markers, and those for 520 μJ/cm^2 are shown with filled markers. (b) Representative fit of OPTP data for an electrolyte-sealed WO$_3$ NP sample. The raw data (blue) markers and best-fit line (red) are displayed. (c) Schematic representation of the components of the electrolyte-sealed samples. Bare WO$_3$ films are prepared on a single quartz substrate.
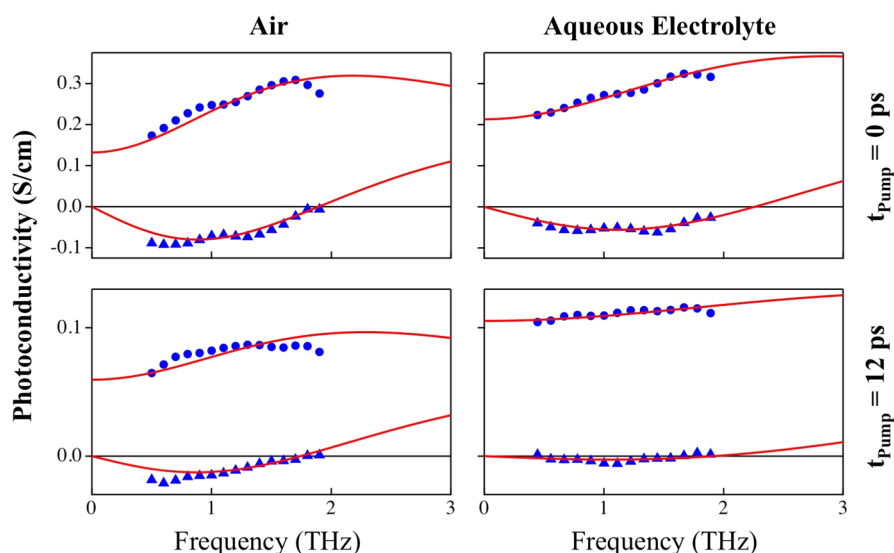
Figure 5. Transient photoconductivity measurements of the WO_3 NP and GP films. An example of the real (circles) and imaginary (triangles) conductivity at different pump delay times is displayed along with the best fit Drude−Smith model (red lines). WO_3 NPs in air and in the presence of aqueous electrolyte photoexcited at 520 $\mu J/cm^2$ of 400 nm light at $t_{pump} = 0$ and $t_{pump} = 12$ ps are presented.

where N is the carrier density, e is the elementary charge of an electron, τ_{scatt} is the carrier scattering time (and is not related to τ in the stretched exponential representing the carrier lifetime), m^* is the effective mass of the electron in WO_3 $(2.4m_e)$,[8] and c_1 is the "persistence of velocity" parameter. The Drude−Smith model accounts for charge carriers that retain some "memory" of their initial velocity prior to a scattering event in the metal oxide and is quantified by the c_1 parameter.[29] When $c_1 = 0$, it reduces to the Drude model, and when $c_1 = -1$, there is complete carrier localization and no net DC transport $(\sigma_0 = 0)$.

The best-fit parameters of eq 3 were found by simultaneously fitting the data to the real and imaginary portion of the frequency-dependent complex conductivity (Figure 5). The best-fit parameters with their associated uncertainties are presented in Table S2. Rather than separately comparing N, τ_{scatt}, and c_1 parameter, it is possible to calculate the net transport, σ_0, and compare it for the 16 permutations of 260 $\mu J/cm^2$ vs 520 $\mu J/cm^2$ excitation fluence, NPs vs GPs, bare films vs electrolyte, and 0 ps vs 12 ps delay time (and also the single configuration at 600 ps delay time).

The current impulse response function is given by[29]

$$j(t)/j(0) = (1 + c_1 t/\tau_{scatt}) \exp(-t/\tau_{scatt}) \quad (4)$$

which means that

$$j(t) \propto N(1 + c_1 t/\tau_{scatt}) \exp(-t/\tau_{scatt}) \quad (5)$$

Since the frequency-dependent complex-valued conductivity is the Fourier transform of the current impulse response function[29]

$$\sigma(\omega) = \int_0^\infty j(t) e^{i\omega t} \, dt \quad (6)$$

we see that the net transport or dc current is given by

$$\sigma_0 \propto \int_0^\infty N(1 + c_1 t/\tau_{scatt}) \exp(-t/\tau_{scatt}) \, dt$$

$$= N \int_0^\infty \exp(-t/\tau_{scatt}) \, dt + N c_1/\tau_{scatt} \int_0^\infty t \exp(-t/\tau_{scatt}) \, dt$$

$$= N\tau_{scatt} + N c_1 \tau_{scatt}$$

$$= N\tau_{scatt}(1 + c_1) \quad (7)$$

Alternatively, evaluating eq 3 with $\omega = 0$ yields

$$\sigma_0 = \frac{Ne^2\tau_{scatt}}{m^*}(1 + c_1) \quad (8)$$

which has the same form as eq 8, but with the advantage that it has conductivity units (S/m) rather than arbitrary units. Figure 6 plots σ_0 for the 16 permutations (and 600 ps). The net
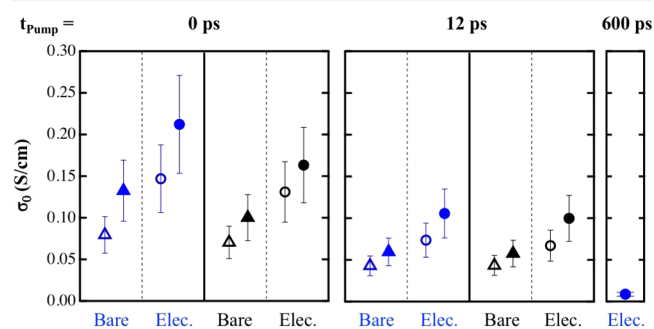

Figure 6. Comparison of WO_3 NPs (blue) and GPs (black), for both bare (triangles) and electrolyte-sealed (circles) samples for 260 $\mu J/cm^2$ (open marker) and 520 $\mu J/cm^2$ (filled marker) pump fluence. The plots display the calculated net transport using eq 8.

transport is higher when the excitation power is higher (filled symbols vs open symbols), but not by a factor of 2. This is not surprising because it has also been previously reported by Klug et al. that the electron/hole recombination has a nonlinear dependence on laser intensity.[13] We assume that a similar trend would exist for the trapping dynamics in the WO_3 valence and conduction bands. Addition of aqueous electrolyte (circles vs

triangles) increases the net transport by nearly a factor of 2 in each case. At t_{pump} = 0 ps, the net transport is slightly higher in the NPs relative to the GPs with 260 $\mu J/cm^2$ fluence and is 30–50% higher in the case of 520 $\mu J/cm^2$ fluence. However, at t_{pump} = 12 ps, the net transport is essentially identical for the NPs and GPs. This is largely due to the values of carrier density, N, shown in Figure S9 and Table S2.

However, a significant difference becomes apparent between the NPs and GPs at very long time scales in the presence of electrolyte. In the case of the NPs, we were able to measure the frequency-dependent conductivity of mobile carriers with delays as long as 600 ps, whereas in the GPs essentially all of the signal is lost by ~200 ps. This is consistent with the OPTP results in Figure 3, which reveal that there is a population of long-lived, mobile carriers in NP sample when immersed in electrolyte. It is apparent from the OPTP best-fit parameters of eq 1 (see Table S1) that the offset, y_0, is 7-fold larger in the NPs compared to the GPs (Figure 7a). We attribute this long time offset to photoinduced carriers that are able to survive far longer than our ~1 ns time window.
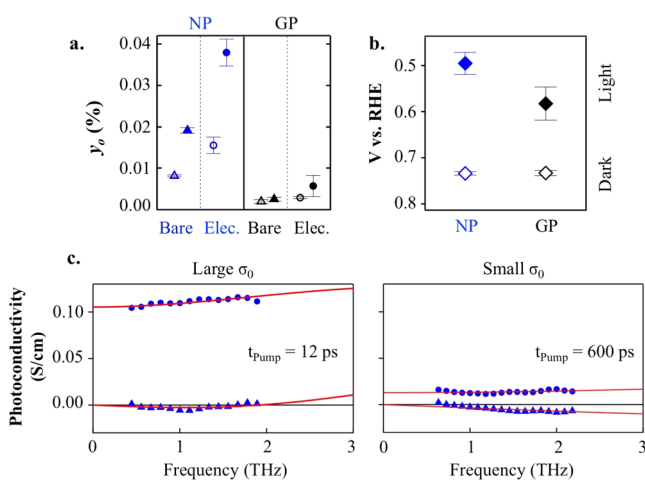
Figure 7. Longer time scale dynamics of WO_3. (a) Amplitude of the long scale dynamics of WO_3 NP (blue) and GP (black) at both 260 $\mu J/cm^2$ (open marker) and 520 $\mu J/cm^2$ (filled marker) pump fluence. (b) Open-circuit photovoltage measurements of the NPs and GPs in a three-electrode photoelectrochemical cell. (c) Emergence of both high and low net transport charge carriers in the WO_3 NPs immersed in aqueous electrolyte at 520 $\mu J/cm^2$ pump fluence.

On the basis of the OPTP and transient photoconductivity results, we believe that the trapping in the NPs depends primarily on the density of traps at the particle surface. Since these particles are essentially single crystalline, the majority of traps exist at the surface and at interparticle interfaces. In the presence of electrolyte, many of these surface traps are passivated, and this leads to a population of long-lived carriers beyond 200 ps. Figure 7c displays the frequency-dependent complex conductivity for t_{pump} = 600 ps. As seen in Table S3, the carrier density of the mobile charges is within a factor of 2 as the early time scale carrier density, yet these long-lived charges are far less mobile due to their reduced scattering time and value of c_1 parameter that is closer to −1. This type of behavior has been observed by Hegmann et al. for the more ordered Si/SiO_2 system where they found a similar trends of localization of photoinduced charge carriers at long time scales.[31]

In contrast to the NPs, we were unable to detect mobile carriers beyond ~400 ps in the GP samples. In this case, the grain boundaries (deep traps) within the GPs have a more significant influence on the amount of long-lived carriers probed with THz radiation compared to surface traps. The influence of grain boundaries on conductivity was studied in a prior report, where it was demonstrated that grain boundaries play a major role on the mobility of charge carriers in other metal oxide semiconductors such as TiO_2.[32]

Taken as a whole, our OPTP and transient conductivity measurements are consistent with the dc conductivity measurements. This correlation suggests that the long-lived carriers in the NPs lead to better overall transport in the NPs relative to the GPs. It is important to note, however, that it is difficult to correlate the ps/ns optical measurements with dc conductivity and photovoltage measurements due to the large differences in the time scale of these measurements. Since trapping in nanostructured materials is a complex process involving many variables, additional work is underway to fully explore the mechanism of trapping as a function of particle size and crystallinity.

Open-Circuit Photovoltage Measurements. Open-circuit photovoltage measurements were carried out using a photoelectrochemical cell with a standard three-electrode configuration to measure the potential of the particle films in the dark and under illumination with a 100 mW/cm^2 AM 1.5G source. The electrolyte and working electrode were both identical to those used in open-circuit OPTP measurements. The equilibrium potentials without illumination at the surface of the NPs and GPs are nearly identical, at 0.73 V vs RHE (see Figure 7b). This is not surprising, given that the flat-band potentials and carrier densities of these materials are approximately equal, and further confirms that the surfaces of the two materials are electrochemically similar in the absence of photoexcitation. Under illumination, the open-circuit photovoltage of the NP and GP films are 0.49 and 0.58 vs RHE, respectively.

The larger photovoltage in the NPs indicates that there is a larger buildup of carriers at longer time scales compared to the GPs. The OPTP and transient photoconductivity measurements may shed some light on the observed difference in the photovoltages of the NPs and GPs. In GPs, photoinduced charge carriers generated within crystallites are much more likely to trap before reaching the surface given the large diameter of the particle and the deep traps present at grain boundaries between crystallites with the particle. Therefore, it is expected that a smaller fraction of carriers will reach the surface in the GPs as compared with the smaller, single-crystalline NPs. In essence, we believe that this is the reason for the correlation between an increase in the long-lived photogenerated carrier concentration, y_0, and the potential difference measured at the WO_3 surface through photoelectrochemical methods.

Much like the dc conductivity measurements, photoelectrochemical measurements are complex and take place on a much longer time scale than ultrafast THz measurements. However, our ultrafast measurements indicate that correlations exist between carrier dynamics and the electrochemical properties of the material, which is an important finding. Future studies examining the ultrafast dynamics under an applied potential will open a wealth of possible comparisons to other photoelectrochemical techniques.[33]

■ CONCLUSION

For the first time, we have investigated the ultrafast photoinduced charge carrier dynamics within crystalline WO_3. Carrier generation yields and early time dynamics are quite similar for the two types of particles (NPs and GPs), and both benefit from passivation of surface states by immersing them in electrolyte. The long time dynamics are significantly different wherein all charge carriers are trapped in the GPs, but a small yet non-negligible fraction survives in the NPs. This results in a significantly larger change in electrode potential under AM 1.5G illumination as well. We therefore recommend material and design strategies that focus on increasing the concentration of low net transport photoinduced mobile charges that survive over long time scales as a means of optimizing photocatalytic activity in WO_3 electrodes.

■ ASSOCIATED CONTENT

Ⓢ Supporting Information

The Supporting Information is available free of charge on the ACS Publications website at DOI: 10.1021/acs.jpcc.6b04390.

> Information on electron microscopy techniques, X-ray diffraction, diffuse reflectance spectroscopy, electrochemistry, and dc conductivity measurements; further explanation of the THz OPTP and transient conductivity measurements (PDF)

■ AUTHOR INFORMATION

Corresponding Author

*E-mail charles.schmuttenmaer@yale.edu, Tel (203) 432-5049 (C.A.S.).

Present Addresses

C.K.: Department of Chemistry, Fordham University, 441 E. Fordham Road, Bronx, NY 10458.
S.W.S.: Catalytic Innovations LLC, 70 Crandall Road, PO Box 356, Adamsville, RI 02801.

Notes

The authors declare no competing financial interest.

■ ACKNOWLEDGMENTS

■ REFERENCES

(1) Grätzel, M. Photoelectrochemical Cells. *Nature* **2001**, *414*, 338−344.

(2) Duan, L.; Tong, L.; Xu, Y.; Sun, L. Visible Light-Driven Water Oxidation- from Molecular Catalysts to Photoelectrochemical Cells. *Energy Environ. Sci.* **2011**, *4*, 3296−3313.

(3) Prévot, M. S.; Sivula, K. Photoelectrochemical Tandem Cells for Solar Water Splitting. *J. Phys. Chem. C* **2013**, *117*, 17879−17893.

(4) Bai, Y.; Mora-Seró, I.; De Angelis, F.; Bisquert, J.; Wang, P. Titanium Dioxide Nanomaterials for Photovoltaic Applications. *Chem. Rev.* **2014**, *114*, 10095−10130.

(5) Swierk, J. R.; Mallouk, T. E. Design and Development of Photoanodes for Water-Splitting Dye-Sensitized Photoelectrochemical Cells. *Chem. Soc. Rev.* **2013**, *42*, 2357−2387.

(6) Zhang, Q.; Uchaker, E.; Candelaria, S. L.; Cao, G. Nanomaterials for Energy Conversion and Storage. *Chem. Soc. Rev.* **2013**, *42*, 3127−3171.

(7) Li, C.; Koenigsmann, C.; Ding, W.; Rudshteyn, B.; Yang, K. R.; Regan, K. P.; Konezny, S. J.; Batista, V. S.; Brudvig, G. W.; Schmuttenmaer, C. A.; Kim, J. H. Facet-Dependent Photoelectrochemical Performance of TiO_2 Nanostructures: An Experimental and Computational Study. *J. Am. Chem. Soc.* **2015**, *137*, 1520−1529.

(8) Chen, R. S.; Wang, W. C.; Lu, M. L.; Chen, Y. F.; Lin, H. C.; Chen, K. H.; Chen, L. C. Anomalous Quantum Efficiency for Photoconduction and Its Power Dependence in Metal Oxide Semiconductor Nanowires. *Nanoscale* **2013**, *5*, 6867−6873.

(9) González-Borrero, P. P.; Sato, F.; Medina, A. N.; Baesso, M. L.; Bento, A. C.; Baldissera, G.; Persson, C.; Niklasson, G. A.; Granqvist, C. G.; Ferreira da Silva, A. Optical Band-Gap Determination of Nanostructured WO_3 Film. *Appl. Phys. Lett.* **2010**, *96*, 061909.

(10) Liu, R.; Lin, Y.; Chou, L. Y.; Sheehan, S. W.; He, W.; Zhang, F.; Hou, H. J. M.; Wang, D. Water Splitting by Tungsten Oxide Prepared by Atomic Layer Deposition and Decorated with an Oxygen-Evolving Catalyst. *Angew. Chem., Int. Ed.* **2011**, *50*, 499−502.

(11) Liu, X.; Wang, F.; Wang, Q. Nanostructure-Based WO_3 Photoanodes for Photoelectrochemical Water Splitting. *Phys. Chem. Chem. Phys.* **2012**, *14*, 7894−7911.

(12) Bedja, I.; Hotchandani, S.; Kamat, P. V. Photoelectrochemistry of Quantized WO_3 Colloids- Electron Storage, Electrochromic, and Photoelectrochromic Effects. *J. Phys. Chem.* **1993**, *97*, 11064−11070.

(13) Pesci, F. M.; Cowan, A. J.; Alexander, B. D.; Durrant, J. R.; Klug, D. R. Charge Carrier Dynamics on Mesoporous WO_3 During Water Splitting. *J. Phys. Chem. Lett.* **2011**, *2*, 1900−1903.

(14) Grigioni, I.; Stamplecoskie, K. G.; Selli, E.; Kamat, P. V. Dynamics of Photogenerated Charge Carriers in $WO_3/BiVO_4$ Heterojunction Photoanodes. *J. Phys. Chem. C* **2015**, *119*, 20792−20800.

(15) Patil, P. S.; Patil, P. R.; Ennaoui, E. A. Characterization of Ultrasonic Spray Pyrolyzed Tungsten Oxide Thin Films. *Thin Solid Films* **2000**, *370*, 38−44.

(16) Ito, S.; Chen, P.; Comte, P.; Nazeeruddin, M. K.; Liska, P.; Péchy, P.; Grätzel, M. Fabrication of Screen-Printing Pastes from TiO_2 Powders for Dye-Sensitised Solar Cells. *Prog. Photovoltaics* **2007**, *15*, 603−612.

(17) Bartel, T.; Gaal, P.; Reimann, K.; Woerner, M.; Elsaesser, T. Generation of Single-Cycle THz Transients with High Electric-Field Amplitudes. *Opt. Lett.* **2005**, *30*, 2805−2807.

(18) Beard, M. C.; Turner, G. M.; Schmuttenmaer, C. A. Transient Photoconductivity in GaAs as Measured by Time-Resolved Terahertz Spectroscopy. *Phys. Rev. B: Condens. Matter Mater. Phys.* **2000**, *62*, 15764−15777.

(19) Beard, M. C.; Turner, G. M.; Schmuttenmaer, C. A. Terahertz Spectroscopy. *J. Phys. Chem. B* **2002**, *106*, 7146−7159.

(20) Kress, M.; Löffler, T.; Eden, S.; Thomson, M.; Roskos, H. G. Terahertz-Pulse Generation by Photoionization of Airwith Laser Pulses Composed of Both Fundamental and Second-Harmonic Waves. *Opt. Lett.* **2004**, *29*, 1120−1122.

(21) Tinkham, M. Energy Gap Interpretation of Experiments on Infrared Transmission through Superconducting Films. *Phys. Rev.* **1956**, *104*, 845−846.

(22) Baxter, J. B.; Schmuttenmaer, C. A. Conductivity of ZnO Nanowires, Nanoparticles, and Thin Films Using Time-Resolved Terahertz Spectroscopy. *J. Phys. Chem. B* **2006**, *110*, 25229−25239.

(23) Jepsen, P. U.; Cooke, D. G.; Koch, M. Terahertz Spectroscopy and Imaging − Modern Techniques and Applications. *Laser Photon. Rev.* **2011**, *5*, 124−166.

(24) Larsen, C.; Cooke, D. G.; Jepsen, P. U. Finite-Difference Time-Domain Analysis of Time-Resolved Terahertz Spectroscopy Experiments. *J. Opt. Soc. Am. B* **2011**, *28*, 1308−1316.

(25) Joint Committee on Powder Diffraction Standards, Card Number 43-1035.

(26) Tang, H.; Prasad, K.; Sanjinès, R.; Schmid, P. E.; Lévy, F. Electrical and Optical Properties of TiO_2 Anatase Thin Films. *J. Appl. Phys.* **1994**, *75*, 2042−2047.

(27) Mi, Q.; Coridan, R. H.; Brunschwig, B. S.; Gray, H. B.; Lewis, N. S. Photoelectrochemical Oxidation of Anions by WO_3 in Aqueous and Nonaqueous Electrolytes. *Energy Environ. Sci.* **2013**, *6*, 2646−2653.

(28) Michalak, D. J.; Gstrein, F.; Lewis, N. S. The Role of Band Bending in Affecting the Surface Recombination Velocities for Si(111) in Contact with Aqueous Acidic Electrolytes. *J. Phys. Chem. C* **2008**, *112*, 5911−5921.

(29) Smith, N. V. Classical Generalization of the Drude Formula for the Optical Conductivity. *Phys. Rev. B: Condens. Matter Mater. Phys.* **2001**, *64*, 155106.

(30) Turner, G. M.; Beard, M. C.; Schmuttenmaer, C. A. In *Ultrafast Phenomena Xiii*; Miller, D. R., Murnane, M. M., Scherer, N. F., Weiner, A. M., Eds.; Springer: 2003; Vol. *71*, pp 331−333.

(31) Titova, L. V.; Cocker, T. L.; Cooke, D. G.; Wang, X.; Meldrum, A.; Hegmann, F. A. Ultrafast Percolative Transport Dynamics in Silicon Nanocrystal Films. *Phys. Rev. B: Condens. Matter Mater. Phys.* **2011**, *83*, 085403.

(32) Wallace, S. K.; McKenna, K. P. Grain Boundary Controlled Electron Mobility in Polycrystalline Titanium Dioxide. *Adv. Mater. Interfaces* **2014**, *1*, 1400078.

(33) Nemes, C. T.; Koenigsmann, C.; Schmuttenmaer, C. A. Functioning Photoelectrochemical Devices Studied with Time-Resolved Terahertz Spectroscopy. *J. Phys. Chem. Lett.* **2015**, *6*, 3257−3262.

Supporting Information

Size-Dependent Ultrafast Charge Carrier Dynamics of WO_3 for Photoelectrochemical Cells

Kevin P. Regan, Christopher Koenigsmann,[a] Stafford W. Sheehan,[b] Steven J.Konezny, and Charles A. Schmuttenmaer*

Department of Chemistry, and Yale Energy Sciences Institute, Yale University, New Haven, CT 06520-8107, United States
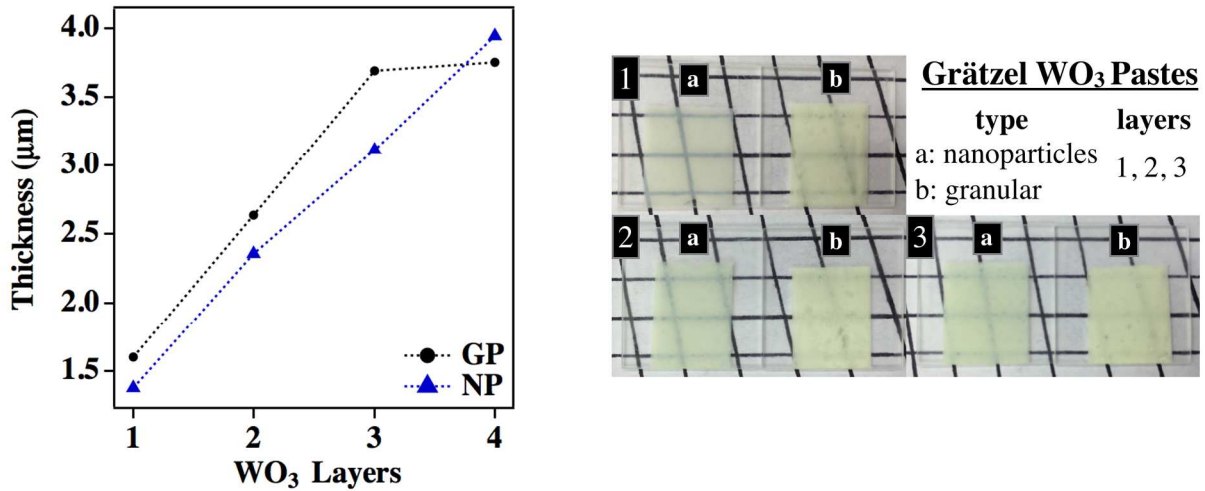[a] Present address: Department of Chemistry, Fordham University, 441 E. Fordham Road, Bronx, NY 10458, United States
[b] Present address: Catalytic Innovations LLC, 70 Crandall Road, PO Box 356, Adamsville, RI 02801, United States
*E-mail: charles.schmuttenmaer@yale.edu, (203) 432-5049

Contents:

1) Characterization of WO₃ Films.

Figure S1: Thicknesses of WO₃ NP (blue) and GP (black) films as a function of the number of doctor bladed layers (left) measured by profilometry. Optical images of films with thicknesses of approximately 1.5 μm (1 layer), 2.5 μm (2 layers) and 3 – 3.5 μm (3 layers) in order to demonstrate their optical transparency.

The average particle size and size distributions of the particles within the sintered films were determined by scanning electron microscopy (SEM) performed on Hitachi SU-70 Analytical Scanning Electron Microscope. The results revealed that the average diameters of the NPs and GPs were 77 ± 34 nm and 390 ± 260 nm, respectively. Histograms of the particle diameter distributions are found in Figure S2. In both cases, the measured diameters were less than the nominal diameters reported by the manufacturer.
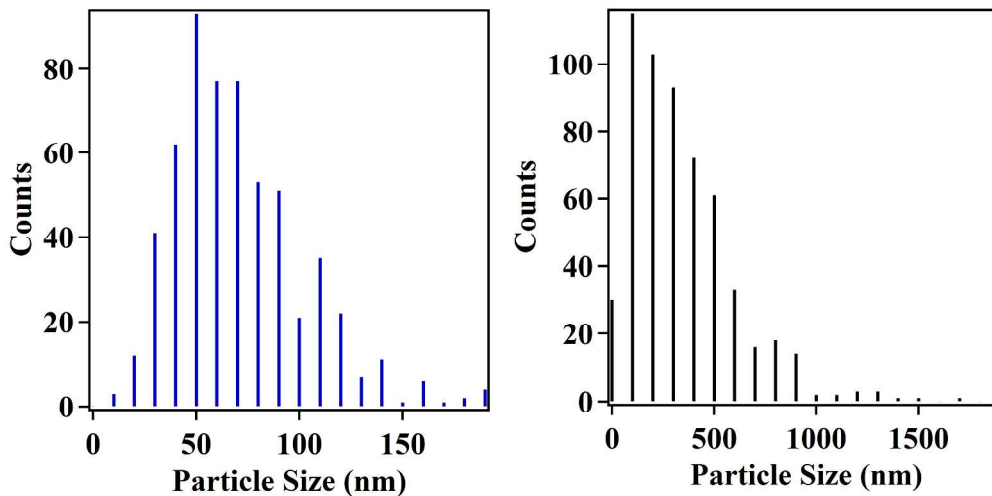

Figure S2: Histograms of the WO₃ particle diameter in the NP (blue) and GP (black) films.

All TEM images were taken on a FEI Technai Osiris 200 kV TEM. The specific surface areas of the as-received WO₃ NP (7.69 m²/g) and GP (0.91 m²/g) powders were determined from nitrogen adsorption isotherms obtained on a QuantaChrome1 porometer utilizing the Brunauer-

Emmett-Teller (BET)[1] method. Before measuring the surface areas, the particles were heated at 120 ℃ for a period of 24 hours to remove excess moisture from the surface.

2) Optical Characterization of WO$_3$ Films.
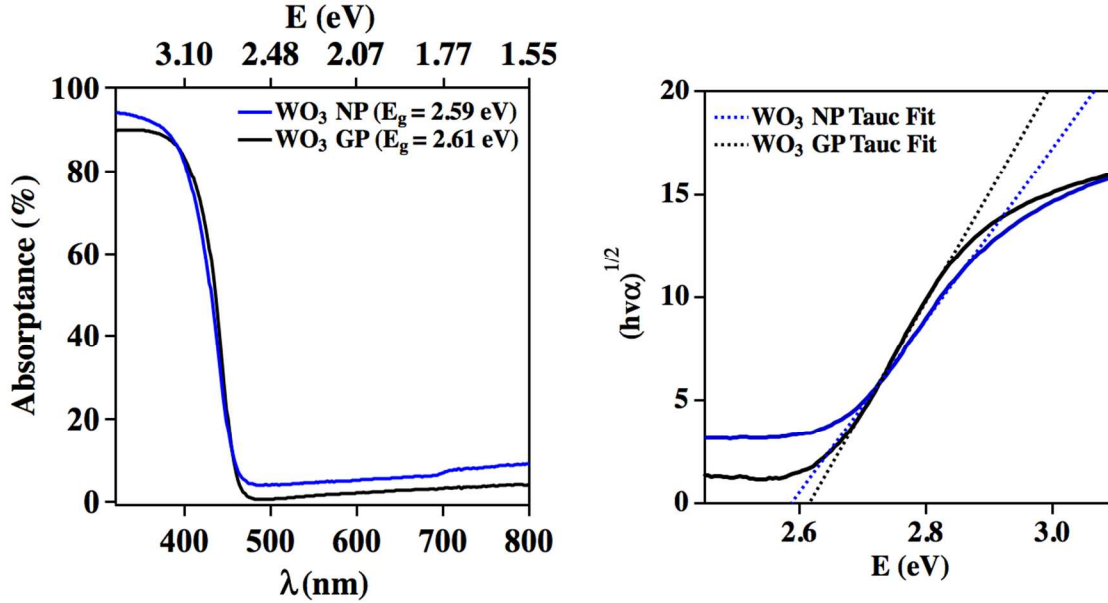
Figure S3: Diffuse reflectance UV-visible measurements were performed to determine the absorptance spectra (left) of WO$_3$ NP and GP films. The band gaps were determined through Tauc plot analysis (right).

Diffuse reflectance spectroscopy was performed with a Shimadzu SU-2600 UV-visible spectrophotometer to determine the optical band gap of the WO$_3$ NP and GP films. The absorptance was found by using a Shimadzu ISR-603 Integrating Sphere to measure the reflectance and transmittance of each sample. The absorptance of the film was calculated from:

$$A = 1 - T - R \tag{S1}$$

where A is the absorptance, T is the transmittance, and R is the reflectance of the film. Tauc plots were prepared as $(Avh)^{1/2}$ vs. E in order to calculate the optical band gap of the NP and GP particles:

$$\left(hv\alpha\right)^{1/n} = A\left(hv - E_g\right) \tag{S2}$$

where h is Planck's constant, v is the frequency of the light, A is the absorptance, α is the absorption coefficient, and $n = 2$ since WO$_3$ is an indirect band gap semiconductor.[2] The region that has a linear dependence on energy is then fit to a straight line. The x-intercept of the fit corresponds to the band gap energy of the sample. The optical band gap of the NPs (E_g = 2.59 eV) and GPs (E_g = 2.61 eV) are nearly identical.

3) X-ray Powder Diffraction (XRD) of WO$_3$ Films.

X-ray diffraction data was collected at room temperature using a Rigaku MicroMax-007HF X-ray source (Cu Kα; λ = 1.54178 Å) coupled to a Saturn 994+ CCD detector. Samples from the WO$_3$ NP and GP films were scraped with oil onto a MiTeGen mount and transferred into an AFC11 goniometer for analysis. After data collection, the Rigaku 2DP software package was used to integrate and process line profiles of the 2D diffraction data, which resulted in the powder diffraction patterns shown in Figure 2e of the main text. The measured diffraction peaks were compared with standard values for monoclinic WO$_3$ from the JCPDS.[3]

4) Time-resolved Terahertz (THz) Spectroscopy.
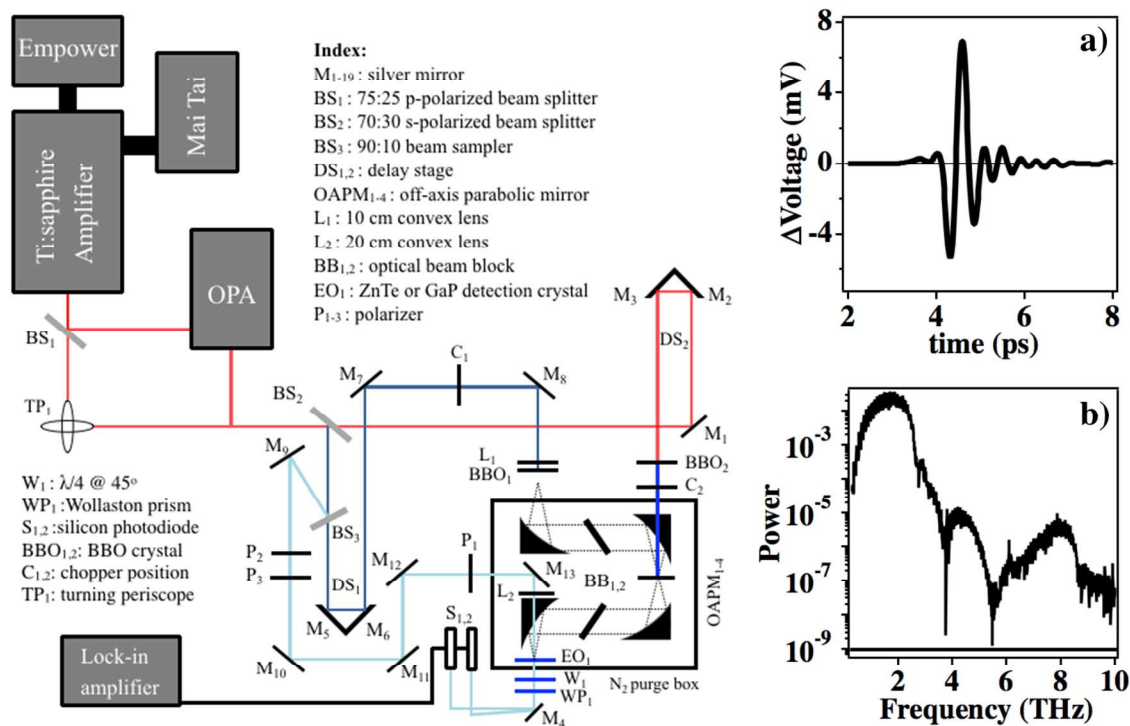
Figure S4: Schematic diagram of the THz spectroscopy setup. The pump beam (red), the generation beam (dark blue), and the detection beam (light blue) are depicted. A THz time-domain (a) pulse and frequency-domain spectrum (b) is shown.

Past studies utilizing time-resolved Terahertz (THz) spectroscopy may be further explored.[4-8] Our current spectrometer setup is presented in Figure S4, and a depiction our experimental bandwidth in Figure S4b.

5) OPTP Scans of Bare and Electrolyte-Sealed WO_3 Films.
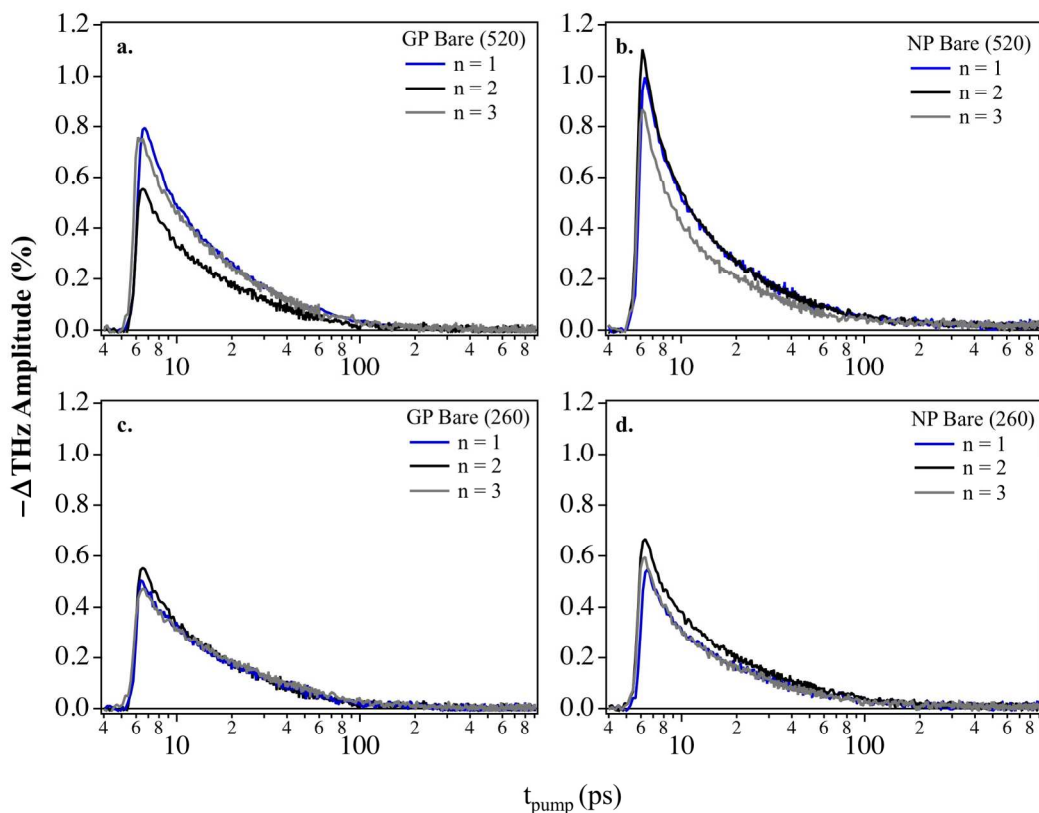
Figure S5: OPTP transients obtained after photoexcitation by a 400 nm pump beam in air. Three samples were used for each particle size (NPs or GPs) and pump fluence (260 or 520 $\mu J/cm^2$).

OPTP transients were taken after photoexcitation by a 260 and 520 $\mu J/cm^2$ optical pump pulse at 400 nm.[4] Each trace consists of an average of 50 transients; from there three different samples prepared under identical conditions were averaged together to yield the traces presented in Figure 3 of the main text. The OPTP transient obtained from each sample was then fit using Equation 1 separately allowing for the determination of the standard deviation of best fit parameters from sample to sample, as seen in Table S1 and S2. Overlays of the raw data confirmed that the trapping dynamics are reproducible from sample-to-sample. The traces in Figure S5-S6 highlight the trapping dynamics from 4 to 900 ps.
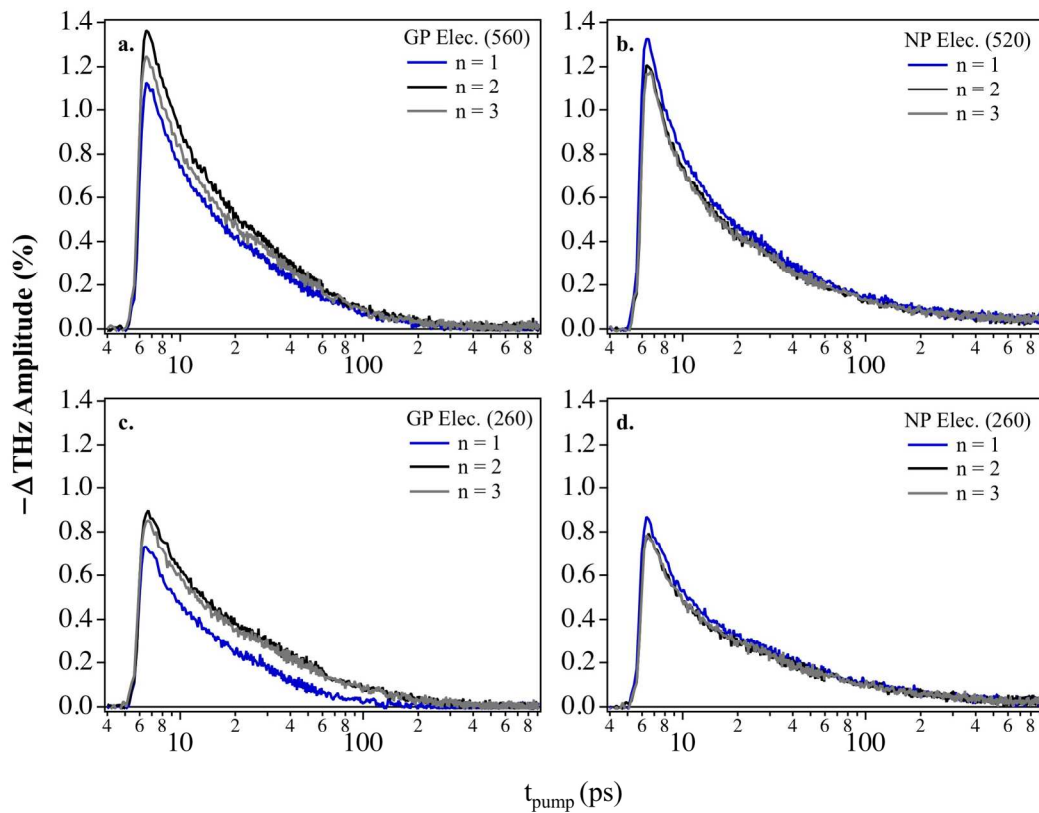
Figure S6: OPTP transients obtained after photoexcitation by a 400 nm pump beam in the presence of 0.1 M NaSO$_4$ (pH = 2). Three samples were used for each particle size (NPs or GPs) and pump fluence (260 or 520 μJ/cm^2).

Table S1. Best fit parameters obtained from the fit of equation 1 to the OPTP transients of both the WO_3 NP and GP in air (Bare).

WO₃ GP/ Bare	F = 520 μJ/cm²	n = 1	n = 2	n = 3	avg.	σ²
	A (%)	1.15	0.86	1.18	**1.06**	0.18
	τ (ps)	5.4	5.0	5.7	**5.3**	0.4
	β (a.u.)	0.45	0.44	0.45	**0.45**	0.00
	t₀ (ps)	5.4	5.8	5.7	**5.6**	0.2
	y₀ (%)	0.003	0.002	0.002	**0.003**	0.001
	χ²	0.321	0.267	0.116	**0.235**	0.107
	FWHM (fs)	577.9	629.5	703.8	**637.1**	63.3
	<τ> (ps)	13.4	12.8	14.3	**13.5**	0.7

WO₃ NP / Bare	F = 520 μJ/cm²	n = 1	n = 2	n = 3	avg.	σ²
	A (%)	1.72	2.06	1.64	**1.81**	0.22
	τ (ps)	2.4	1.8	1.8	**2.0**	0.4
	β (a.u.)	0.37	0.36	0.37	**0.37**	0.01
	t₀ (ps)	5.9	5.7	5.7	**5.7**	0.1
	y₀ (%)	0.019	0.019	0.020	**0.019**	0.001
	χ²	0.297	0.247	0.275	**0.273**	0.025
	FWHM (fs)	581.6	697.3	591.5	**623.5**	64.2
	<τ> (ps)	9.9	8.2	7.4	**8.5**	1.3

WO₃ GP/ Bare	F = 260 μJ/cm²	n = 1	n = 2	n = 3	avg.	σ²
	A (%)	0.62	0.58	0.64	**0.61**	0.03
	τ (ps)	9.6	8.4	8.5	**8.8**	0.6
	β (a.u.)	0.49	0.47	0.52	**0.49**	0.03
	t₀ (ps)	5.6	5.6	5.5	**5.6**	0.1
	y₀ (%)	0.003	0.002	0.002	**0.002**	0.001
	χ²	0.259	0.340	0.332	**0.310**	0.044
	FWHM (fs)	680.1	726.5	643.7	**683.4**	41.5
	<τ> (ps)	19.9	18.8	15.9	**18.2**	2.1

| WO₃ NP / Bare	F = 260 μJ/cm²	n = 1	n = 2	n = 3	avg.	σ²
	A (%)	0.85	1.14	1.03	**1.01**	0.14
	τ (ps)	3.7	3.0	2.5	**3.1**	0.6
	β (a.u.)	0.39	0.37	0.38	**0.38**	0.01
	t₀ (ps)	5.9	5.7	5.6	**5.7**	0.1
	y₀ (%)	0.008	0.008	0.008	**0.008**	0.0002
	χ²	0.280	0.215	0.278	**0.258**	0.037
	FWHM (fs)	613.4	647.7	638.0	**633.0**	17.7
	<τ> (ps)	13.0	12.7	10.1	**11.9**	1.6

Table S2. Best fit parameters obtained from the fit of Equation 1 to the OPTP transients of both the WO_3 NP and GP in in 0.1 M $NaSO_4$ electrolyte with a pH of 2 (Elec.).

	F = 520 μJ/cm²	n = 1	n = 2	n = 3	**avg.**	σ^2
WO_3 GP/ Elec.	A (%)	1.64	2.03	1.74	**1.80**	0.20
	τ (ps)	7.1	7.0	8.2	**7.4**	0.7
	β (a.u.)	0.44	0.43	0.46	**0.44**	0.01
	t_o (ps)	5.8	5.7	5.7	**5.8**	0.0
	y_o (%)	0.003	0.007	0.008	**0.006**	0.003
	χ^2	0.419	0.549	0.707	**0.558**	0.144
	FWHM (fs)	739.2	684.8	739.9	**721.3**	31.6
	$<\tau>$ (ps)	18.5	18.8	19.6	**19.0**	0.6

	F = 520 μJ/cm²	n = 1	n = 2	n = 3	**avg.**	σ^2
WO_3 NP / Elec.	A (%)	2.59	2.54	2.14	**2.42**	0.25
	τ (ps)	2.0	1.8	2.6	**2.2**	0.4
	β (a.u.)	0.30	0.30	0.32	**0.31**	0.01
	t_o (ps)	5.80	5.81	5.88	**5.83**	0.04
	y_o (%)	0.036	0.036	0.042	**0.038**	0.003
	χ^2	0.734	0.521	0.449	**0.568**	0.148
	FWHM (fs)	697.0	657.8	621.8	**658.9**	37.6
	$<\tau>$ (ps)	19.2	17.0	18.5	**18.2**	1.1

	F = 260 μJ/cm²	n = 1	n = 2	n = 3	**avg.**	σ^2
WO_3 GP/ Elec.	A (%)	0.92	1.24	1.20	**1.12**	0.17
	τ (ps)	9.4	9.9	9.6	**9.6**	0.2
	β (a.u.)	0.56	0.43	0.43	**0.47**	0.08
	t_o (ps)	5.5	5.5	5.5	**5.5**	0.0
	y_o (%)	0.0000	0.0004	0.0005	**0.0003**	0.0002
	χ^2	0.511	0.517	0.558	**0.529**	0.026
	FWHM (fs)	665.8	630.8	704.1	**666.9**	36.7
	$<\tau>$ (ps)	15.6	27.7	27.1	**23.5**	6.8

	F = 260 μJ/cm²	n = 1	n = 2	n = 3	**avg.**	σ^2
WO_3 NP / Elec.	A (%)	2.33	1.88	1.73	**1.98**	0.31
	τ (ps)	0.8	1.2	1.6	**1.2**	0.4
	β (a.u.)	0.24	0.26	0.27	**0.26**	0.01
	t_o (ps)	5.52	5.88	5.87	**5.76**	0.21
	y_o (%)	0.013	0.017	0.016	**0.016**	0.002
	χ^2	0.437	0.466	0.413	**0.439**	0.027
	FWHM (fs)	690.03	745.84	750.20	**728.7**	33.55
	$<\tau>$ (ps)	22.8	22.0	23.8	**22.9**	0.9
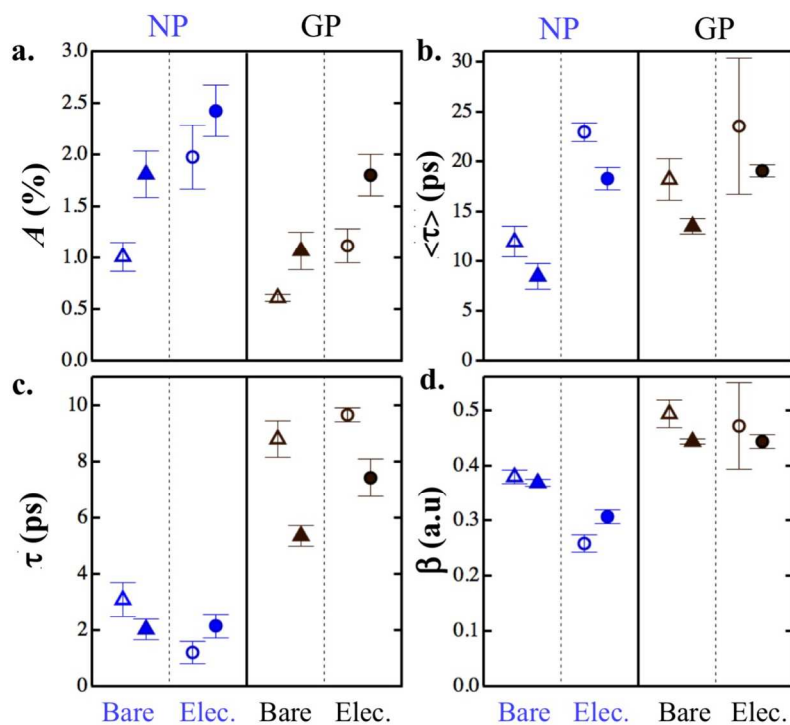
Figure S7: Parts a, b, c and d) depict the best fit parameters for the stretched exponential trapping dynamics of WO_3 NPs (blue) and GPs (black). The parameters for data taken at 260 $\mu J/cm^2$ excitation fluence are shown with open markers, and at 520 $\mu J/cm^2$ are shown with filled markers. Error bars indicate 1σ standard deviation obtained from three different samples.
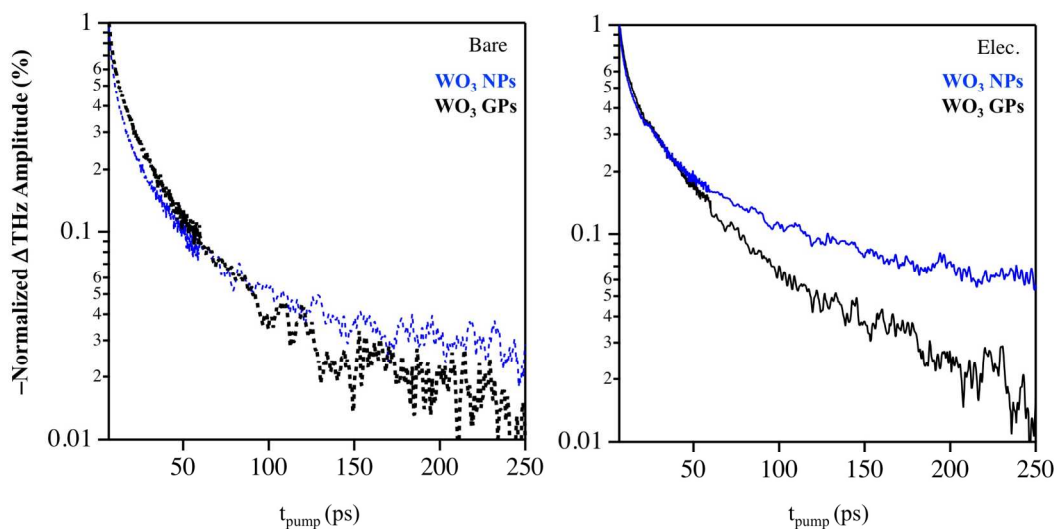
Figure S8: Normalized OPTP transients obtained at 520 $\mu J/cm^2$ displayed in a semi-logarithmic plot to qualitatively show the change in the stretching parameter between samples in air vs. electrolyte.

6) Transient Photoconductivity of WO$_3$ Films Probed with THz Radiation.

The advantage of using THz spectroscopy to determine the transient conductivity of the sample is that it is a non-contact probe with sub-picosecond temporal resolution, and it determines the complex-valued, frequency-dependent conductivity of the sample.[5,6,8] The ratio between the Fourier transform of the photoexcited, E_{pump} (ω, t_{Pump}), and the nonphotoexcited, E_{ref} (ω), time-domain waveforms yields the transient transmission function:[9,10]

$$\hat{T}\left(\omega, t_{pump}\right) = \frac{E_{pump}\left(\omega, t_{pump}\right)}{E_{ref}\left(\omega\right)} = \frac{n\left(\omega\right)+1}{n\left(\omega\right)+1+Z_0\hat{\sigma}\left(\omega, t_{pump}\right)\delta} \quad . \tag{S5}$$

This expression can be rearranged to determine the complex conductivity, $\hat{\sigma}$:

$$\hat{\sigma}\left(\omega, t_{pump}\right) = \frac{n\left(\omega\right)+1}{Z_0\delta}\left(\frac{1}{\hat{T}\left(\omega, t_{pump}\right)} - 1\right), \tag{S4}$$

where $n(\omega)$ is the refractive index of the substrate that the THz pulse experiences, Z_o is the impedance of free space, and δ the skin depth of the material. The skin depth of the WO$_3$ for 400 nm light is 3 µm.[11] The refractive index of quartz in the THz region is 2.1.[12] The real and imaginary frequency-dependent conductivities of the WO$_3$ films are shown in Figure S8.
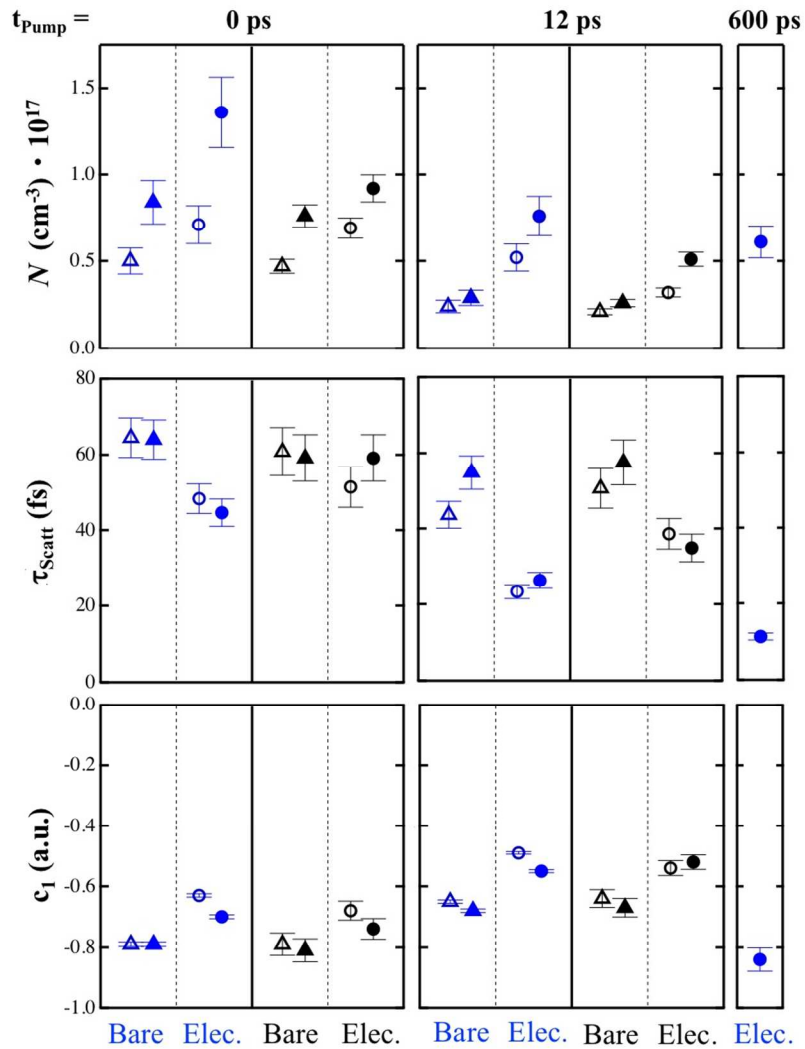
The frequency-dependent conductivity is determined without having to choose a conductivity model. However, it is useful to employ a model when interpreting the experimental results. The Drude model of conductivity is most commonly used, but as is the case with many nanomaterials, the WO$_3$ NPs and GPs do not exhibit Drude-like behavior; therefore the Drude-Smith which is presented in Equation 3 of the main text. The calculated real and imaginary conductivity and the best fit parameters are presented in Figure S9.
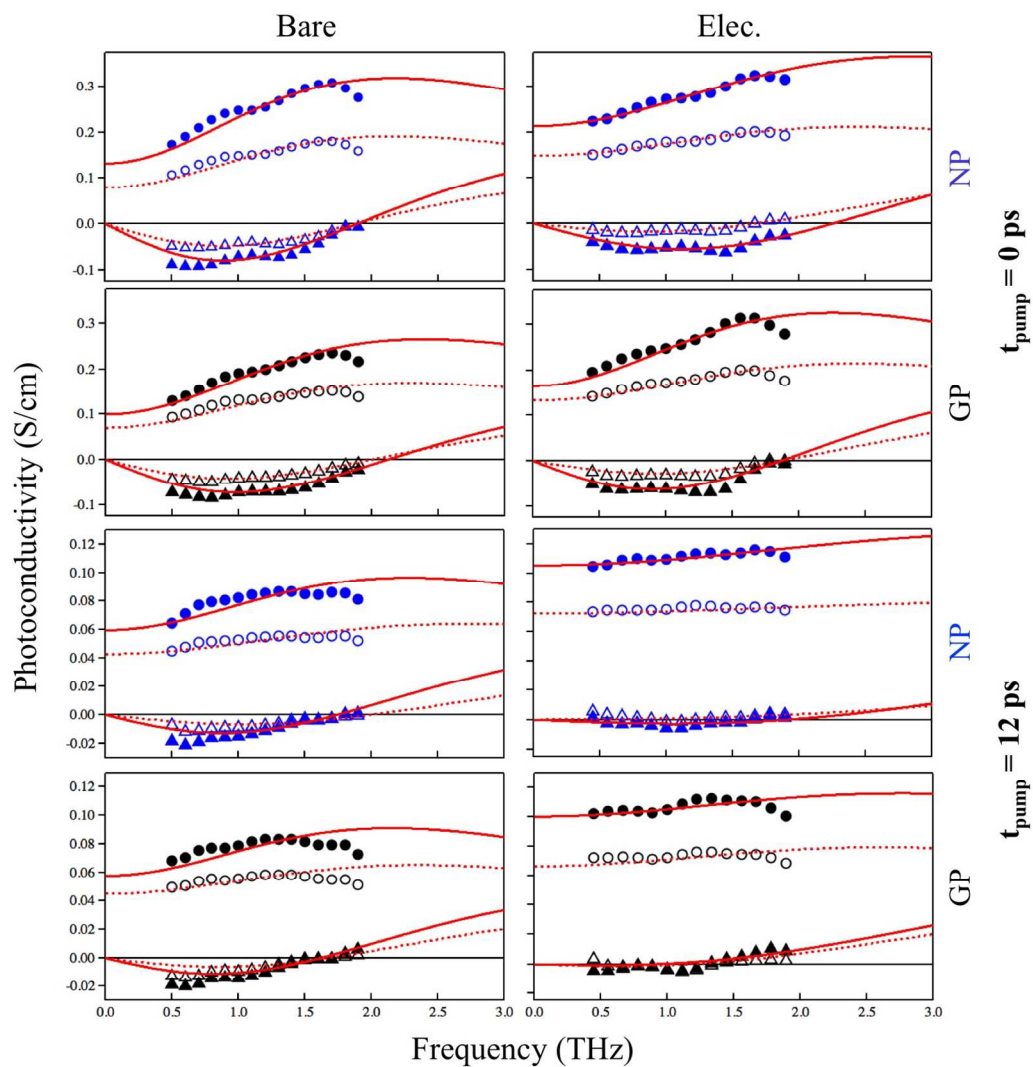
Figure S9: Transient photoconductivity measurements of WO$_3$ NPs (blue) and GPs (black) at 520 μJ/cm^2 (closed marker) and 260 μJ/cm^2 (open marker) pump fluence in air and 0.1 M NaSO$_4$ (pH = 2) electrolyte. The real (circles) and imaginary (triangles) portions of the complex photoconductivity are displayed. The best-fit Drude-Smith parameters (red) are extended from 0 – 3 THz.

Table S3. Best fit parameters obtained from the global fit of equation 3 to the transient photoconductivity traces. All of these values are displayed in Figures 6 and 7 of the main text. Each column is labeled by its type (NP or GP) and pump fluence (260 or 520 $\mu J/cm^2$).

Bare WO$_3$		NP-520	NP-260	GP-520	GP-260
t_{pump} = 0 ps	N (cm^{-3}) • 10^{17}	0.84	0.50	0.76	0.47
	τ (fs)	64.0	64.5	59.1	60.8
	μ (cm2/V s)	46.9	47.3	43.3	44.6
	c (a.u)	-0.79	-0.79	-0.81	-0.79
	σ_o (S/cm)	0.133	0.080	0.100	0.070
	χ^2	0.0058	0.0028	0.0045	0.0024
t_{pump} = 12 ps		NP-520	NP-260	GP-520	GP-260
	N (cm^{-3}) • 10^{17}	0.29	0.24	0.26	0.21
	τ (fs)	54.8	43.6	57.5	50.6
	m (cm2/V s)	40.2	32.0	42.1	37.1
	c (a.u)	-0.68	-0.65	-0.67	-0.64
	σ_o (S/cm)	0.060	0.043	0.058	0.043
	χ^2	0.0058	0.0011	0.0003	0.0006
Elec. / WO$_3$		NP-520	NP-260	GP-520	GP-260
t_{pump} = 0 ps	N (cm^{-3}) • 10^{17}	1.36	0.71	0.92	0.69
	τ (fs)	44.6	48.3	59.1	51.4
	m (cm2/V s)	32.7	35.4	43.3	37.7
	c (a.u)	-0.70	-0.63	-0.74	-0.68
	σ_o (S/cm)	0.212	0.147	0.163	0.131
	χ^2	0.0016	0.0004	0.0001	0.0022
t_{pump} = 12 ps		NP-520	NP-260	GP-520	GP-260
	N (cm^{-3}) • 10^{17}	0.76	0.52	0.51	0.32
	τ (fs)	26.3	23.3	34.9	38.6
	m (cm2/V s)	19.3	17.1	25.6	28.3
	c (a.u)	-0.55	-0.49	-0.52	-0.54
	σ_o (S/cm)	0.106	0.074	0.100	0.067
	χ^2	0.0001	0.0008	0.0004	0.0003
		NP-520			
t_{pump} = 600 ps	N (cm^{-3}) • 10^{17}	0.61			
	τ (fs)	8.7			
	m (cm2/V s)	8.2			
	c (a.u)	-0.86			
	σ_o (S/cm)	0.009			
	χ^2	0.0001			

Figure S10: Best fit parameters for the Drude-Smith model. WO_3 NPs (blue) and GPs (black), for both bare (triangles) and electrolyte-sealed (circles) samples are compared. The plots display parameters at time-zero injection and twelve picoseconds after photoexcitation, each for 260 $\mu J/cm^2$ (open marker) and 520 $\mu J/cm^2$ (filled marker) pump fluence. For the WO_3 NPs sealed with electrolyte, the transient conductivity was measured 600 ps after photoexcitation.

7) Efficiency of Photogenerated Charge Carriers.

Transient conductivity data were taken with a 400 nm optical pump pulse using fluences, F, of 260 and 520 μJ/cm^2 (100 and 200 μJ of pulse energy with a ~7 mm diameter excitation beam size). The maximum theoretical carrier density generated by the pulse characteristics given above is ~1.75 × 10^{18} cm^{-3} and ~3.5 × 10^{18} cm^{-3} when using a skin depth of 3 μm. However, reflection losses of ~15% must be taken into account which reduces the photoexcited carrier density to ~1.5 × 10^{18} cm^{-3} and 3 × 10^{18} cm^{-3}, respectively.

It is noted that when we probe dynamics at t_{pump} = 0 ps, the actual amplitude is convoluted with our instrument response function which makes reduces it by a factor of two. There is also a large uncertainty in the effective mass of the carriers in WO$_3$. We found only a single literature value, and it is from 1970 and could easily be a factor of two too low. Finally, given that the thickness of the film is about 3 microns, it might be more appropriate to use the refractive index of the non-photoexcited material (which is 6) in the thin-film formula (Equation S4) rather than the index of the substrate (which is 2.1). This would increase the carrier density by a factor of 2.3. Overall, the carrier densities extracted from the Drude-Smith analysis should be increased by a factor of 2 × 2 × 2.3 = 9.2 and compared to the experimental values that include reflection losses. The quantum efficiency of carrier generation based on these considerations is reported in Table S4.

Table S4. Calculation of the efficiency of photoinduced charge carriers compared to the theoretical approximation. Each column is labeled by its type (NP or GP) and pump fluence (260 or 520 μJ/cm^2).

<div align="center">

Quantum Efficiency (%)

Dielectric Medium	NP-520	NP-260	GP-520	GP-260
WO$_3$ Bare	25.8	30.6	23.2	28.8
WO$_3$ Elec.	41.6	43.6	28.2	42.4

</div>

The discrepancy between the theoretical carrier density and those determined from the Drude-Smith model could be due to carriers that are photoexcited directly into trap states. Future work will investigate these issues since so little is known about the optical and electronic properties of WO$_3$.

8) No Influence of Electrolyte with 400 nm Excitation.
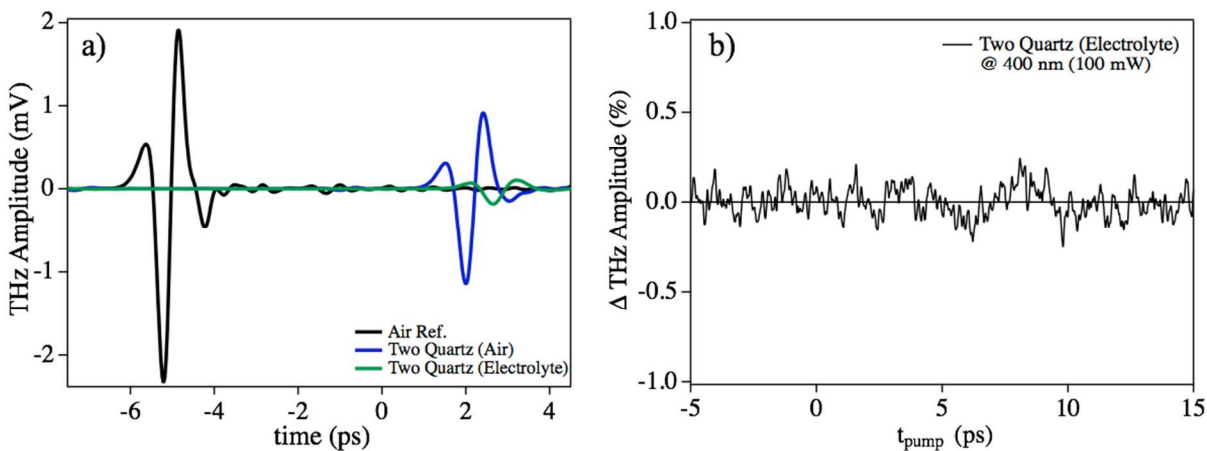
Figure S11: a) Depiction of the THz time-domain pulse passing through air (black), two quartz slides with 25 μm of air, and two quartz slides with 25 μm of 0.1 M Na_2SO_4 (pH = 2). b) There is no change in THz amplitude when only the electrolyte is photoexcited with 400 nm light at 260 μJ/cm^2.

Figure S11 verifies that the electrolyte has no influence on the OPTP signal. The change in dynamics that we observe with the introduction of electrolyte is completely due to a change in the material properties of the WO_3 when electrolyte is introduced.

8) Calculation of the Flat Band Potential.
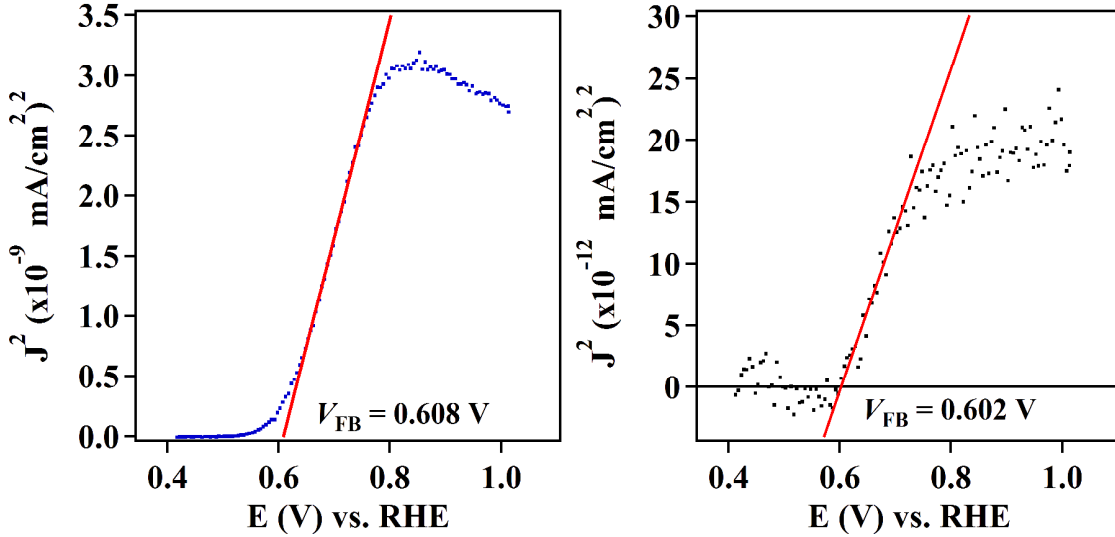
Figure S12: Butler plots obtained in 0.1 M Na_2SO_4 at a pH of 2 for the NPs (a) and the GPs (b). The data have been corrected for an instrumental offset before fitting.

Electrochemical measurements were taken using a WaveNow XV potentiostat (Pine) in a standard three-electrode configuration. The WO_3 films doctor-bladed on an FTO-coated glass (TEC 15, Hartford Glass) electrode were used as working electrodes, with an Ag/AgCl reference electrode (Bioanalytical Systems, Inc) and Pt mesh counter electrode. A two-chamber cell was used for all electrochemical measurements, with the working electrode, reference electrode, and quartz window for illumination in one chamber, and the Pt mesh counter electrode in the other. The chambers were separated by a glass frit. The flat band potential was calculated for WO_3 NPs and GPs as a control to demonstrate that their surface electrochemical properties are approximately equivalent. Therefore, the difference in activity for water oxidation is attributed to the difference in the particle size relative to the charge diffusion length, rather than from differences in the concentration of surface states that may be intrinsic to the synthetic procedures used to make them.

The flat band potentials were determined by measuring steady-state catalytic current densities (dwell time of 2 seconds per mV) under monochromatic illumination (λ = 400 nm, at 1 mW/cm^2), and following the methods outlined by Butler.[13] In short, when $\alpha L_p \ll 1$ (where α is the absorption coefficient and L_p is the hole diffusion length), as is the case for WO_3 under 400 nm illumination, the relationship between the potential applied to the electrode and photocurrent becomes:

$$V - V_{FB} \approx \left(\frac{J}{\alpha W_0 q \varphi_0} \right) \qquad (S5)$$

where V is the applied voltage, V_{FB} is the flat band potential, J is the measured current, q is the charge transferred, ϕ is the photon flux, and W_o is the depletion width at a constant potential of 1 V. This allows us to determine the flat-band potential for the WO_3 NP and GP films by plotting J^2 vs V, as seen in figure S12.

9) Dark DC Conductivity Measurements

The WO_3 NP and GP films for the electrical conductivity measurements were prepared on sapphire substrates using the paste preparation, film deposition, and thermal annealing methods described in the main text. Gold electrical contacts with a chromium adhesion layer were deposited on top of the films using a thermal evaporator. Current-voltage characteristics in the range of 0 to 1 V were obtained on an Agilent B1500A semiconductor device analyzer equipped with medium-power source-measurement units paired with atto-sense and switch units for high-resolution current sensing. The ambient conductivity was measured repeatedly for up to, and sometimes exceeding, 24 hours in order to determine a steady state value.

10) Supplementary References.

(1) Brunauer, S.; Emmett, P. H.; Teller, E. Adsorption of Gases in Multimolecular Layers. *J. Am. Chem. Soc.* **1938**, *60*, 309-319.

(2) Tauc, J.; Grigorov.R; Vancu, A. Optical Properties and Electronic Structure of Amorphous Germanium. *Phys. Status Solidi* **1966**, *15*, 627-637.

(3) Joint Committee on Powder Diffraction Standards, Card Number 43-1035.

(4) Beard, M. C.; Turner, G. M.; Schmuttenmaer, C. A. Terahertz Spectroscopy. *J. Phys. Chem. B* **2002**, *106*, 7146-7159.

(5) Beard, M. C.; Turner, G. M.; Schmuttenmaer, C. A. Transient Photoconductivity in GaAs as Measured by Time-Resolved Terahertz Spectroscopy. *Phys. Rev. B* **2000**, *62*, 15764-15777.

(6) Beard, M. C.; Turner, G. M.; Schmuttenmaer, C. A. Size-Dependent Photoconductivity in CdSe Nanoparticles as Measured by Time-Resolved Terahertz Spectroscopy. *Nano Lett.* **2002**, *2*, 983-987.

(7) Turner, G. M.; Beard, M. C.; Schmuttenmaer, C. A. In *Ultrafast Phenomena Xiii*; Miller, D. R., Murnane, M. M., Scherer, N. F., Weiner, A. M., Eds. 2003; Vol. 71, p 331-333.

(8) Turner, G. M.; Beard, M. C.; Schmuttenmaer, C. A. Carrier Localization and Cooling in Dye-Sensitized Nanocrystalline Titanium Dioxide. *J. Phys. Chem. B* **2002**, *106*, 11716-11719.

(9) Larsen, C.; Cooke, D. G.; Jepsen, P. U. Finite-Difference Time-Domain Analysis of Time-Resolved Terahertz Spectroscopy Experiments. *J. Opt. Soc. Am. B* **2011**, *28*, 1308-1316.

(10) Tinkham, M. Energy Gap Interpretation of Experiments on Infrared Transmission through Superconducting Films. *Phys. Rev* **1956**, *104*, 845-846.

(11) Deb, S. K. Optical and Photoelectric Properties and Colour Centres in Thin Films of Tungsten Oxide. **1973**, *27*, 801-822.

(12) Bründermann, E., Hübers, Heinz-Wilhelm, Kimmitt, Maurice FitzGerald *Terahertz Techniques*; Springer Series in Optical Sciences, 2012.

(13) Butler, M. A. Photoelectrolysis and Physical Properties of the Semiconducting Electrode WO_2 *J. Appl. Phys.* **1977**, *48*, 1914-1920.